

# A Method for Evaluating Frequency Regulation in an Electrical Grid – Part II: Applications to Non-Synchronous Devices

Álvaro Ortega, *Member, IEEE*, Federico Milano, *Fellow, IEEE*

**Abstract**—The second part of this two-part paper discusses how to determine whether a device connected to the grid is providing inertial response and/or frequency control. The proposed technique is based on the index proposed in Part I of this paper. This part first discusses the dynamic behavior in terms of the rate of change of controlled power of a variety of non-synchronous devices that do and do not regulate the frequency. These include passive loads, energy storage systems and thermostatically controlled loads. Then a case study based on a real-world dynamic model of the all-island Irish transmission system discusses an application, based on a statistical analysis, of the proposed technique to wind power plants with and without frequency control. The properties and the robustness with respect to noise and other measurement issues of the proposed technique are also thoroughly discussed.

**Index Terms**—Primary frequency control, inertial response, converter-interfaced generation, phasor measurement unit (PMU), wind turbines, energy storage.

## I. INTRODUCTION

The trend in the last decade of substituting conventional power plants with non-synchronous devices is well known. This trend poses several issues for the dynamic response and control of power systems [1]–[3]. The ability of non-synchronous devices to provide frequency control is thus well assessed. However, there is no direct way to this date to verify whether a given device is actually providing frequency control at a given time or not. This is a major concern for system operators and prevents relying on and properly rewarding the devices that provide such frequency support. Smart metering is already a reality but it is mostly utilized on the device side to implement the frequency control itself, e.g. [4], rather than on the system operator side. This second part of the paper focuses on a particular aspect, namely, the provision of frequency control by non-synchronous and non-conventional devices.

Recent studies discuss the potential of non-synchronous generation for frequency control. These studies consider several technologies, including wind generation [5]–[7], solar

photovoltaic (PV) generation [8]–[10], Voltage Sourced Converters - High Voltage Direct Current (VSC-HVDC) links [11], energy storage devices [12]–[14], and thermal loads [15]–[17].

In Part I of this two-part paper, we have derived the mathematical formulation of the concept of Rate of Change of Power (RoCoP),  $\dot{p}'_{\mathbb{B}}(t)$ , and its link with the frequency deviation at system buses,  $\Delta\omega_{\mathbb{B}}(t)$ . For convenience, this expression is recalled below:

$$\dot{p}'_{\mathbb{B},h}(t) = \sum_{k \in \mathbb{B}} \hat{B}_{\text{bus}}^{hk} [\Delta\omega_{\mathbb{B},h}(t) - \Delta\omega_{\mathbb{B},k}(t)], \quad (1)$$

where  $\mathbb{B}$  is the set of network buses and  $\hat{B}_{\text{bus}}^{hk}$  is the susceptance of the branch connecting bus  $h$  to bus  $k$  multiplied by the synchronous reference angular speed in rad/s. As discussed in Part I, from the RoCoP, one can also estimate the regulating power at the bus, as follows:

$$\begin{aligned} \Delta p'_{\mathbb{B},h}(t) &= \int_t \dot{p}'_{\mathbb{B},h}(\tau) d\tau \\ &= \int_t \sum_{k \in \mathbb{B}} \hat{b}_{hk} [\Delta\omega_{\mathbb{B},h}(\tau) - \Delta\omega_{\mathbb{B},k}(\tau)] d\tau. \end{aligned} \quad (2)$$

In this second part, we first focus on two specific features of the RoCoP, namely, (i) the ability to differentiate between devices that have and do not have an impact on the frequency at their point of connection; and (ii) the estimation of the equivalent inertia of non-synchronous devices coupled to fast Primary Frequency Control (PFC). These points are illustrated through three devices, namely, passive (constant admittance) loads, energy storage systems, and thermostatically controlled loads.

Then, the main contribution of the second part of this paper is presented and discussed, namely a statistical approach to evaluate the inertial response and fast frequency regulation provided by non-synchronous devices, such as wind power plants. The accuracy, robustness and applicability of the proposed technique is validated by means of a comprehensive case study based on the dynamic model of the All-Island Irish Transmission System (AIITS) [18]. The size of this system (1,479 buses) and the high penetration of Converter-Interfaced Generation (CIG) make this system an excellent test-bed to evaluate the features of the proposed RoCoP-based estimation technique.

The steady-state power-flow data of the AIITS are available at the official website of the Irish system operator, EirGrid Group. Dynamic data were guessed based on the technology

Á. Ortega is with LOYOLATech, Universidad Loyola Andalucía, Spain. F. Milano is with the AMPSAS research group, School of Elec. and Electron. Eng., University College Dublin, Ireland. E-mails: aortega@uoyola.es; federico.milano@ucd.ie

This work is supported by the European Commission and by the Spanish Ministry of Science by funding Á. Ortega under projects FLEXITRANSTORE – H2020-LCE-2016-2017-SGS-774407 and ENE2017-88889-C2-1-R, respectively. This material is also based upon works supported by the European Commission and the Science Foundation Ireland by funding F. Milano under the Project EdgeFLEX, grant no. 883710, and under the Investigator Programme award, project AMPSAS, grant no. SFI/15/IA/3074, respectively.

of the generators but allowed to achieve a remarkable fidelity with the dynamic response behavior of the actual system. The interested reader can refer to [19], where the authors compare real-world measurements provided by EirGrid Group with the dynamic model of the system that has been set up in the simulation platform used to run the simulations presented and discussed in this paper.

The remainder of Part II of the paper is organized as follows. The models of non-conventional devices providing PFC that are discussed in this paper are briefly described in Section II. Section III discusses the proposed statistical approach based on the RoCoP. Section IV discusses the behavior of the RoCoP and equivalent inertia for a selection of non-synchronous devices. The case study based on the AIITS is presented in Section V. Finally, Section VI provides conclusions and outlines future work directions.

All results discussed in Sections IV and V were obtained using Dome [20] and were executed on a 64-bit Linux Ubuntu 18.04 operating system running on an 8 core 3.40 GHz Intel® Core i7™ with 16 GB of RAM.

## II. MODELS OF FREQUENCY-CONTROLLING DEVICES

This section presents the schemes of the PFC loops of devices other than synchronous machines (SMs), namely Energy Storage Systems (ESSs), Thermostatically-Controlled Loads (TCLs) and Wind Energy Conversion Systems (WECSs) in Subsections II-A, II-B and II-C, respectively [21]. The frequency measured at the bus of connection of these devices is assumed to be obtained through Synchronous Reference Frame PLLs (SRF-PLLs). The model of such devices and their accuracy is discussed in Section V.B of Part I.

### A. Energy Storage Systems

A simple Proportional-Integral-Derivative (PID)-based Fast Frequency Response (FFR) of converter-interfaced ESSs is depicted in Fig. 1 [13]. Note that we purposely make a distinction, based on their time scales, between PFC (i.e. from about 5 s after a contingency) and FFR (i.e. from tens of milliseconds after a contingency). For FFR purposes, only ESSs that are connected to the main grid through power converters are relevant. For this reason, in the remainder of this paper, we use the term ESSs to refer to converter-interfaced ones. The dependency on time of the variables included in the control schemes have been omitted in the remainder of this paper for compactness.

The input of the regulator is the error between the measured frequency at the bus of connection,  $\omega_{B,h}(t)$ , and its reference set-point,  $\omega^{\text{ref}}$ . The controller gives as output the variable of the storage device that regulates its active power output,  $u$ , (e.g. the duty cycle of the dc/dc converter of a battery, or the rotor angular speed of a flywheel). The frequency error is passed through a deadband block and a Low-Pass Filter (LPF) in order to reduce the sensitivity of the storage control to small, high-frequency perturbations. The output of the LPF,  $x_{f,u}(t)$ , is then used as input of two channels, one for the droop control with gain  $\alpha$ , and one for the Rate of Change of Frequency (RoCoF) control, which computes the derivative of the filtered frequency error  $x_r(t)$  by means of a washout filter.

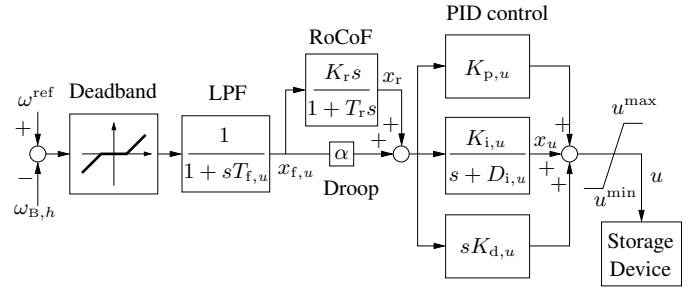


Fig. 1: Fast frequency control scheme of a ESS.

### B. Thermostatically-Controlled Loads

TCLs are dynamic loads with temperature control. These can be air conditioning systems, industrial refrigerators or heating systems. In most cases, the reference temperature is fixed to an assigned value. There are, however, prototypes of TCLs that include a measure of the system frequency and that vary the reference temperature in order to reduce frequency deviations [22]–[24]. The control scheme of the TCL is depicted in Fig. 2.

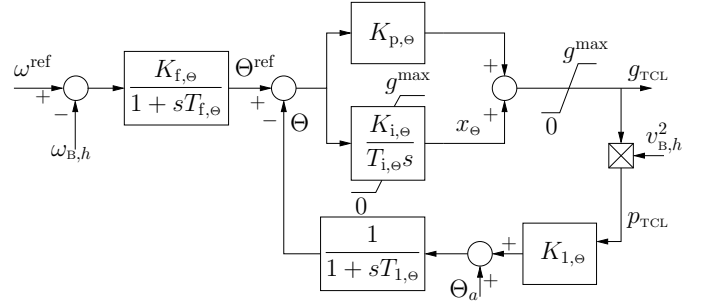


Fig. 2: Scheme of the primary frequency control of a TCL.

The meaning of the variables is as follows:  $\Theta(t)$  and  $\Theta_a(t)$  are the load (lumped model) and ambient temperatures, respectively;  $g_{\text{TCL}}(t)$  is the equivalent load conductance;  $v_{B,h}(t)$  is the voltage at the load bus; and  $p_{\text{TCL}}(t)$  the active power consumed by the TCL.  $g^{\text{max}}$  is defined as  $g^{\text{max}} = K_L g_0$ , where  $g_0 = \frac{p_0}{v_0^2}$  is the equivalent conductance at rated power and voltage; and  $K_L$  is the ceiling conductance output ratio.  $K_L < 1$  for cooling systems and  $K_L > 1$  for heating systems.

### C. Wind Energy Conversion Systems

The FFR scheme of WECSs considered in this paper is shown in Fig. 3 [5], [25], [26].

The resulting control signal  $\Delta p_w(t)$  is the sum of the output of the droop and RoCoF controllers, which is then added to the active power reference obtained from the Maximum Power Point Tracking (MPPT),  $p_w^*(t)$ . Each channel of the frequency controller is expected to operate at different time scales after a contingency. The RoCoF control acts in the first instants after the occurrence of a contingency due to its sensitivity to the rate of change  $\Delta \dot{\omega}_{B,h}(t)$ , while the frequency deviation  $\Delta \omega_{B,h}(t)$  is more effective to mitigate the frequency nadir. Hence, the two control channels are expected to be complementary.

## III. STATISTICAL INTERPRETATION OF THE ROCOP

In Part I, we have proposed a taxonomy of devices based on their ability to vary the frequency at their point of connection

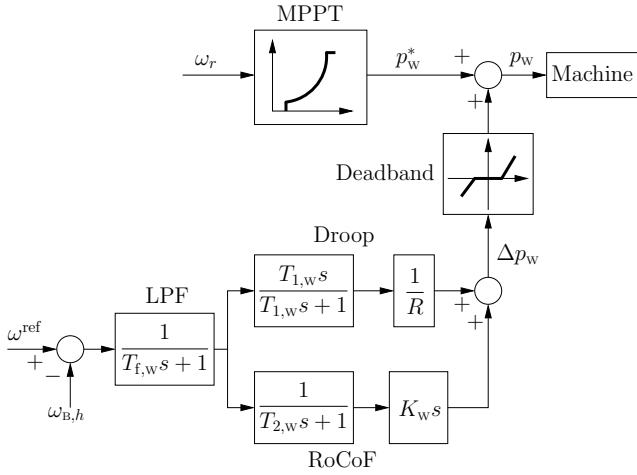


Fig. 3: Fast frequency control scheme of a WECS.

with the grid. In particular, a device is assumed to be able to modify the frequency if it satisfies the following condition on the RoCoP (see also the discussion of eq. (24) of Part I of this paper):

$$|\dot{p}'_{B,h}(t)| \approx \left| \frac{\Delta p_{B,h}(t)}{\Delta t} \right| \geq \epsilon, \quad (3)$$

where  $\epsilon > 0$  is an empirical threshold. A detailed description of the taxonomy of devices that do and do not modify the frequency locally can be found in Section III of Part I of this paper.

The definition of the threshold  $\epsilon$  has to take into account the dynamic behavior of the device. In the taxonomy given in Part I, we have discussed that this can be done considering the rate of change and the magnitude of the power variations. Based on that, we further discuss two relevant cases: (i) stochastic fluctuations of the power source, such as the wind speed; and (ii) measurement noise.

The statistical properties of the wind can be properly determined based on time series of wind speed measurements [27], [28]. Similarly, the volatility of other renewable energy resources can be studied through stochastic differential equations, e.g., the effect of clouds on the solar irradiance [29] and of the swell phenomenon on tidal currents [30]. The most relevant information from these models is the standard deviation of the fluctuations and the autocorrelation coefficient. The latter indicates, on a statistical basis, how much the wind speed is going to change from one value to another in a given time. Roughly speaking, the autocorrelation coefficient of a stochastic process is the equivalent of the time constant of a first-order differential equation [31].

From the standard deviation of the stochastic process, one can adjust the value of the threshold  $\epsilon$  in (3). On the other hand, the references above indicate that the autocorrelation of the stochastic processes of renewable sources leads to variations whose time scales are either slower (e.g., clouds and swell phenomenon) or faster (e.g., wind short-term fluctuations) than the FFR and are naturally filtered by the turbines and/or the regulators of the Distributed Energy Resources (DERs). Similarly, the noise of the measurements of the bus frequencies tends to be much faster than the inertial response and

FFR. Such a noise can thus be filtered without affecting the reliability of the RoCoP. The case study extensively illustrates the effect of both stochastic fluctuations of the source and measurement noise.

#### IV. EXAMPLES BASED ON NON-SYNCHRONOUS DEVICES

This section discusses the behavior of the RoCoP and the estimation of equivalent inertias for non-synchronous devices that do not include noise or whose noise is small enough to be easily decoupled from the effect of the regulation. These examples are based on the well-known Western Systems Coordinating Council (WSCC) 9-bus system [32] and complete the illustrative example on the synchronous machines and their conventional frequency regulators presented in Part I of this paper. In the following, we discuss passive loads (Example 1), and ESSs and TCLs (Example 2).

##### A. Example 1: Passive Loads

Loads are equally as important as generators for the transient analysis of power systems. For transient stability studies such as those presented in this paper, a passive load connected at the transmission or distribution level is commonly modeled as a constant admittance, as follows:

$$p_{B,h}(t) = p_{B,ho} v_{B,h}^2(t), \quad q_{B,h}(t) = q_{B,ho} v_{B,h}^2(t), \quad (4)$$

where  $v_{B,h}(t)$  is the voltage magnitude at the bus  $h$  where the load is connected;  $p_{B,h}(t) + jq_{B,h}(t)$  is the complex power consumption at the load bus; and the subscript  $o$  denotes the power at the nominal voltage.

During a transient, the power consumption varies quadratically with the voltage magnitude  $v_{B,h}(t)$ . However, such power variations are not due to either intrinsic variations nor a regulation of the load. Instead, they are due to the evolution of the overall system following the contingency. Thus, the RoCoP and consequently the regulating power of passive constant admittances is negligible. This is illustrated in Fig. 4, that shows the RoCoP index and power variations of the load at bus 8 following the loss of load considered in Example 1.

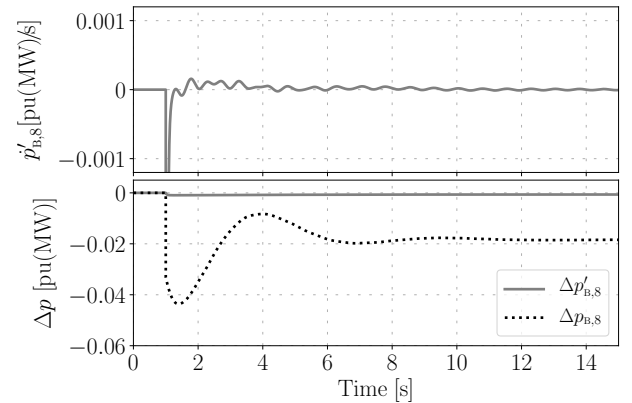


Fig. 4: WSCC system – RoCoP  $\dot{p}'_{B,8}(t)$  and estimated active power variations of the passive load at bus 8.

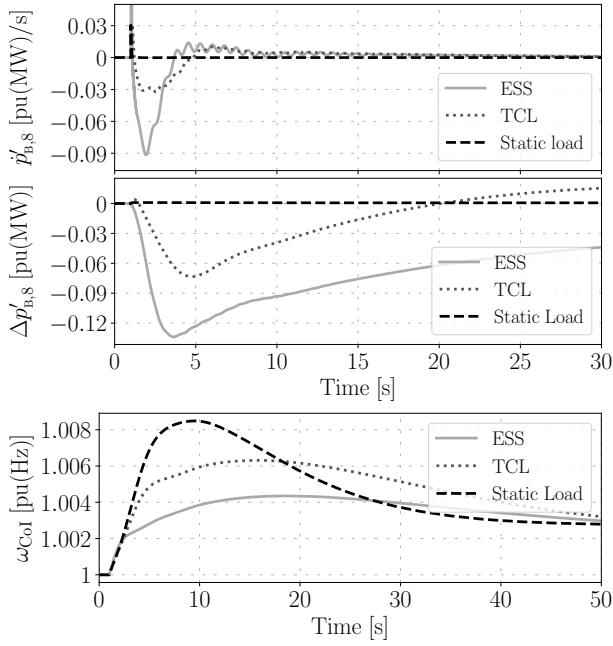


Fig. 5: WSCC system – RoCoP  $\dot{p}'_{B,8}(t)$ , regulating power variations at bus 8, and frequency of the CoI with and without an ESS or a TCL regulating the local frequency.

### B. Example 2: ESSs and TCLs

In this example, we compare two families of devices, namely ESSs and TCLs [13], [23]. These devices show substantially different response times with respect to the PFC of synchronous machines: the ESSs is faster (tens-hundreds of milliseconds) and the TCLs is slower (several seconds).

Figure 5 shows the RoCoP, the regulating power estimation and the frequency of the Center of Inertia (CoI) when an ESS or a TCL is connected to bus 8. The ESS models a battery storage system [13], and it is connected to bus 8 in antenna through an auxiliary bus, namely bus 8\*. The TCL represents 25% of the total load of bus 8. In this scenario, PFC is included in all machines, and the contingency considered is again the outage of 20% of the load at bus 5. Both speed and size of the active power variations after the disturbance affect the RoCoP. The difference between power nadirs is less than 50% and the zenith difference of the RoCoP  $\dot{p}'_{B,8}(t)$  is about 70%. The ESS has a higher RoCoP than the TCL, and this leads to a significant improvement of the transient response of the system.

The accuracy of the regulating power estimation is validated next. If the control that regulates the ESS active power output,  $p_{ESS}(t)$ , is designed to provide FFR then, in steady-state conditions,  $p_{ESS,o} = 0$ , thus:

$$\Delta p_{B,8^*}(t) = p_{ESS}(t) - p_{ESS,o} = p_{ESS}(t). \quad (5)$$

Figure 6 shows that the trajectories of  $\Delta p_{B,8^*}(t)$  and  $\Delta p'_{B,8^*}(t)$  (the latter calculated with (2)) are fairly similar. The small offset (about 4%) that can be observed for  $t > 5$  s is due to the fact that (1) and, hence, (2), do not take into account transmission line losses, nor voltage-driven power variations.

Figure 7 shows the RoCoP and the actual and estimated ESS regulating power with and without a deadband applied to

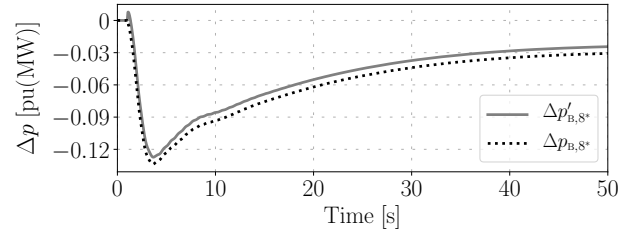


Fig. 6: WSCC system – Variations of regulating power injection and active power output of the ESS regulating the frequency at bus 8\*.

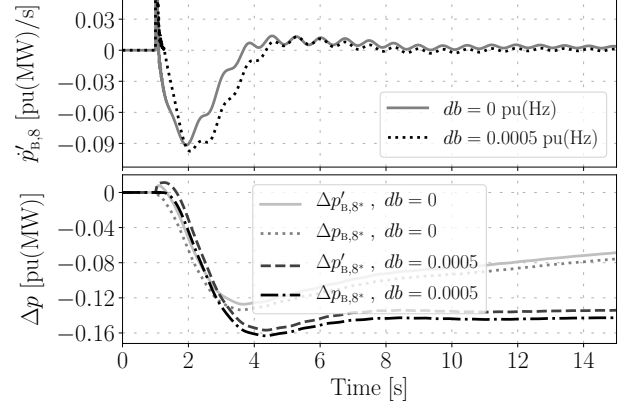


Fig. 7: WSCC system – Regulating power injection at bus 8\* and ESS active power output with deadband regulating the local frequency.

the frequency error signal used as input of the ESS frequency control loop [13]. The inclusion of a 30 mHz deadband (0.0005 pu) introduces a delay in the response of the ESS, which results in a larger amount of power (and thus, of energy) stored by the device. The accuracy of the estimated ESS active power output is not affected by the inclusion of the deadband.

Finally, the equivalent inertia of both the ESS and the TCL is estimated by means of equation (32) of Part I, which is recalled below in (6), and results are displayed in Fig. 8:

$$M_{\blacksquare,h}(t) \approx \frac{-\dot{p}'_{B,h}(t)}{d^2/dt^2 \left[ \Delta\omega_{B,h}(t) - \hat{x}_{\blacksquare,h} \dot{p}'_{B,h}(t) \right]}, \text{ for } t < t'. \quad (6)$$

LPFs are required to filter out the signals from the numerical issues due to the sudden jumps observed in the upper panel of Fig. 5 when the loss of load occurs. An equivalent internal reactance of 1 pu( $\Omega$ ) is considered in both cases. A time constant for the LPFs of 1 s has been used in the estimation.

As expected, the ESS shows a considerably higher equivalent inertia than the TCL right after the loss of the load. The response of the FFR of the ESS rapidly leads to cancel the two terms in the denominator of equation (6), thus causing the singularity observed at  $t \simeq 2.8$  s. The slower response of the TCL delays the occurrence of such a singularity. Note that (6) is only valid in the time scale of the typical machine inertial response ( $t \lesssim 1$  s), and cannot be used in other time scales (e.g. in steady-state or for long term dynamics).

Note that the singularity of the estimated inertia seen in Fig. 8 has no physical meaning. On the other hand, the main information that can be extracted is that while synchronous machines have a constant inertia, non-synchronous devices,

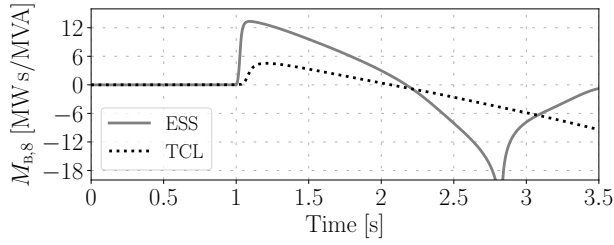


Fig. 8: WSCC system – Estimated inertia of an ESS and a TCL connected to bus 8.

although not providing physical inertia, can actually provide during a transient and through their control an equivalent inertia, which, however, is not constant, reaching its maximum in the first instants after a contingency. A noteworthy result of the proposed estimation technique is that it allows quantifying such inertia and thus enables the comparison of different devices and controllers.

## V. CASE STUDY

The case study presented in this section consists of four parts. The description of the AIITS is provided in Subsection V-A. Section V-B discusses the ability of the proposed RoCoP to detect the frequency regulation of non-synchronous generation, in particular, wind power plants. This section also illustrates the capability of the RoCoP to discriminate between WECSs that do or do not provide FFR. This is done by studying the statistical variations of the power injections that are due to variations of the wind speed and those that are a result of the FFR provided by the WECSs. The non-linear behavior of converter-interfaced generation operating near its rated power is studied in Section V-C. Finally, Section V-D discusses the tuning of RoCoP filtering to reduce impact of the stochastic fluctuations of the wind speed as well as of Phasor Measurement Unit (PMU) measurement noise on the reliability of the RoCoP.

### A. System Description

The dynamic model of the AIITS includes 1,479 buses, 1,851 branches, 245 loads modeled as constant admittances during transients and as constant power injections in quasi-steady-state conditions, 22 conventional synchronous power plants modeled with 6<sup>th</sup> order SM models with d-axis saturation, Automatic Voltage Regulations (AVRs) and turbine governors, 6 Power System Stabilizers (PSSs), and 176 wind power plants, 34 of which are equipped with Constant-Speed (CSIG) and 142 with Doubly-Fed Induction Generatorss (DFIGs). The topology and the steady-state data of the AIITS are made publicly available by the Irish TSO, EirGrid Group. Dynamic data are guessed based on power plant technologies.

While all system is simulated, we focus on a region of the AIITS that includes an SM, four wind power plants, and four loads. The scheme of this region and its connections with the rest of the grid are shown in Fig. 9. The devices connected to buses A through E are as follows.

- 1) Bus A – SM of 55 MW capacity and starting time  $M_G = 16.282$  kWs/kVA.

- 2) Bus B – DFIG-based wind power plant generating 23 MW at initial conditions.
- 3) Bus C – DFIG-based wind power plant generating 23 MW at initial conditions coupled to FFR.
- 4) Bus D – DFIG-based wind power plant generating 3 MW at initial conditions.
- 5) Bus E – CSIG-based wind turbine generating 0.25 MW at initial conditions.

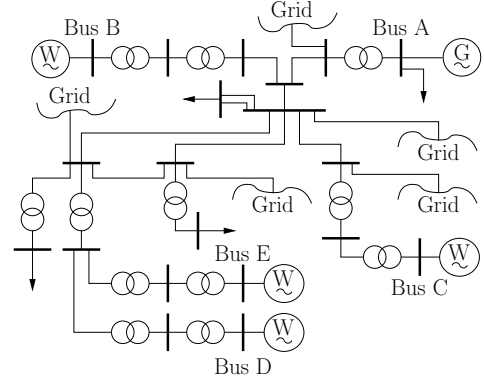


Fig. 9: Section of the AIITS.

All wind power plants include stochastic wind fluctuations. The stochastic differential equations that model the Weibull-distributed processes are given in [28] while wind parameters are from [27]. Since the time scale of interest is that of the inertial response and primary frequency control, we assume that the wind speed has a fast exponentially decaying autocorrelation, as thoroughly discussed in [27].

### B. Case 1: Stochastic Generation

This section discusses the tuning of the threshold  $\epsilon$  of (3) to identify the wind power plants that regulate the frequency at their point of connection with the grid. No filtering of the RoCoP is considered in this section. The threshold, hereinafter indicated with  $\epsilon_{WT}$ , has to be defined based on the knowledge of the system, e.g., through statistical moments such as the standard deviation of the RoCoP,  $\dot{p}'_{B,h}(t)$ , of a device or subsystem connected to a particular bus over an adequate time period. As discussed in Section III of Part I, one does not need to know the specific nature of the device/subsystem connected at bus  $h$  to define  $\epsilon_{WT}$ , as (1) is calculated exclusively through network measurements.

Figure 10 shows the estimation of the RoCoP for the WECSs connected to buses B, C and D. 1,000 trajectories of 120 s of duration with a time step of 20 ms have been generated with different wind profiles, and no FFR is implemented in any WECS. The top panel shows the histograms of the trajectories at the end of the simulations, whereas the bottom panel shows the Probability Density Function (PDF)-fit of each histogram to a normal distribution with zero average and standard deviations:

$$\begin{aligned} \sigma_{\dot{p}'_{B,B}} &= 2.18 \cdot 10^{-3} \text{ pu(MW)/s} , \\ \sigma_{\dot{p}'_{B,C}} &= 3.14 \cdot 10^{-3} \text{ pu(MW)/s} , \\ \sigma_{\dot{p}'_{B,D}} &= 4.24 \cdot 10^{-4} \text{ pu(MW)/s} . \end{aligned}$$

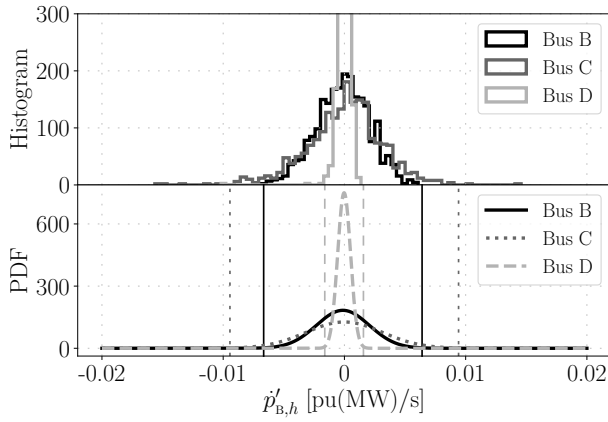


Fig. 10: AIITS – Histogram and PDF of the RoCoP  $\dot{p}'_{B,h}(t)$  at buses B, C and D for 1,000 trajectories. WECSs do not include FFR. The vertical lines indicate the value of  $\pm 3\sigma_{p'_{B,h}}$ .

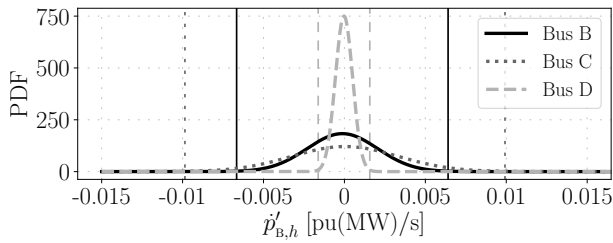


Fig. 11: AIITS – PDF of the RoCoP  $\dot{p}'_{B,h}(t)$  at buses B, C and D for 1,000 trajectories. WECS at bus C includes FFR. The vertical lines indicate the value of  $\pm 3\sigma_{p'_{B,h}}$ .

Consistently, WECSs with larger capacities lead to higher standard deviations. For example, WECS at bus D shows a  $\sigma_{p'_{B,D}}$  about an order of magnitude smaller than  $\sigma_{p'_{B,B}}$  and  $\sigma_{p'_{B,C}}$ . Less expectedly, WECSs with same technology and capacity, i.e. those connected at buses B and C, show significantly different  $\sigma_{p'_{B,h}}$  (about 30%). This is due to various factors: (i) the topology of the grid where the WECS is connected; (ii) the geographical location of the WECS and the wind profile that is characteristic of that location; and (iii) the number of wind turbines in operation within the WECS in the considered time period. Therefore, the effectiveness of the FFR provided by a WECS does not depend only on its capacity. The RoCoP can thus be a valuable index for system operators as it allows taking into account the topological, geographical and technical aspects discussed above.

Figure 11 shows the PDF-fit of the RoCoP at buses B, C and D when FFR is implemented in the WECS at bus C. Wind variations are not large enough to trigger the FFR, and thus,  $\sigma_{p'_{B,C}}$  shows a fairly similar value as for the case without FFR:  $\sigma_{p'_{B,C}} = 3.29 \cdot 10^{-3}$  pu(MW)/s. This is an expected result from the discussion presented in Subsections III-A.2 and III-B.2 in Part I.

Figure 12 shows the trajectories of the RoCoP at buses B, C and D (top panel), and the variations of the active power injected and regulating power at buses B and C (bottom panel) for a single trajectory with stochastic wind perturbations and FFR implemented at bus C. In this case, the simulation lasts 300 s with a time step of 50 ms. This integration step is used

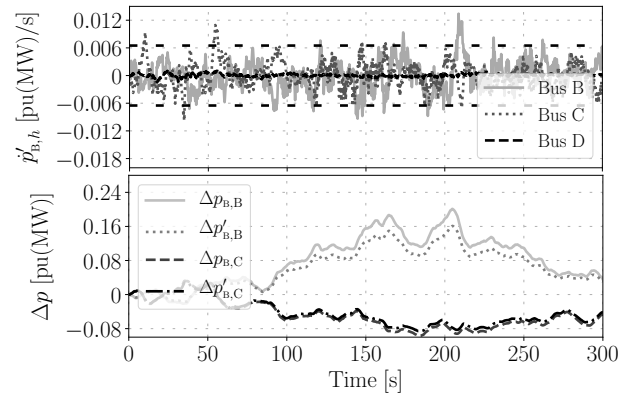


Fig. 12: AIITS – Trajectories of the RoCoP  $\dot{p}'_{B,h}(t)$  at buses B, C and D; and variations of the active power injected and equivalent regulating power at buses B and C. WECS at bus C includes FFR.

in the remainder of this case study.

The statistical analysis discussed above and illustrated in Figs. 10 and 11 is used to define the threshold  $\epsilon_{WT}$  that sets the boundaries to identify whether a device is participating in the regulation of the local frequency or not. Given the normal distributions provided in both figures, it can be assumed that, for more than 99% of the time in normal operating conditions, the RoCoP will lie within the thresholds  $\pm 3\sigma_{p'_{B,h}}$ . Individual thresholds can thus be easily defined for each wind power plant considered. However, and for the sake of illustration, comparison and discussion, one single threshold based on  $\sigma_{p'_{B,B}}$  is defined for all plants in the scenarios analyzed below.

By setting  $\pm\epsilon_{WT} = \pm 3\sigma_{p'_{B,B}} \approx \pm 6.5 \cdot 10^{-3}$  pu(MW)/s (see the horizontal dashed lines in the top panel of Fig. 12), one can safely infer that the WECS at bus D does not impact on the frequency at its point of connection. As expected from the discussion above, the indexes  $\dot{p}'_{B,B}(t)$  and  $\dot{p}'_{B,C}(t)$  are, for most of the time, within the thresholds  $\pm\epsilon_{WT}$ . As no contingency occurs during the simulated time, it is not trivial to infer, not from the RoCoP neither from the active power variations, that one of the wind power plants includes FFR and the other one does not. This is due to the fact that, under normal conditions, the output reference of the FFR is null or almost null, specially if deadbands and filters are applied.

Figure 13 shows the results for a loss of a 44 MW, 13.2 MVar load occurring at  $t = 50$  s. In this case, the RoCoP clearly indicates that the WECS at bus C is providing FFR as observed from the values of  $\dot{p}'_{B,C}(t)$  in the few seconds after the contingency. This is not so clear from the active power injection shown in the bottom panel of the figure. After  $t = 50$  s,  $\Delta p'_{B,C}(t)$  shows a ramp that, in magnitude, is smaller than other ramps observed in  $\Delta p'_{B,B}(t)$  (see e.g. the variations for  $t \in [160, 220]$  s).

Figure 14 shows a closeup of 20 seconds around the occurrence of the loss of the load, where the RoCoP and the difference of frequency variations between the WECS bus and the neighboring bus are depicted. The RoCoP at bus B, which does not include FFR, does not surpass the thresholds  $\pm\epsilon_{WT}$ . On the other hand, the RoCoP at bus C, which does include FFR, goes beyond  $\epsilon_{WT}$  by about six times during the first half of the oscillation after the contingency, and by about three

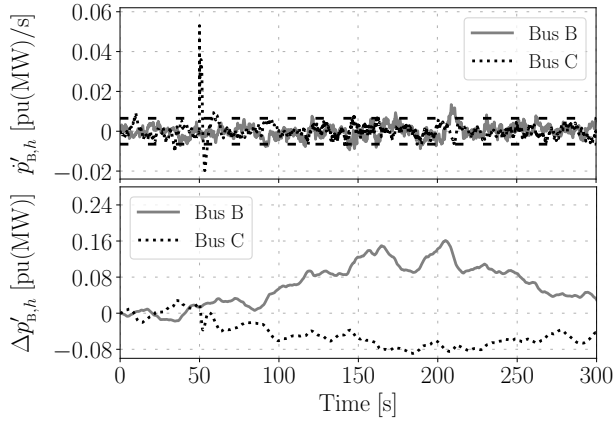


Fig. 13: AIITS – Trajectories of the RoCoP  $\dot{p}'_{B,h}(t)$  and estimated equivalent regulating power at buses B and C following a loss of load. WECS at bus C includes FFR.

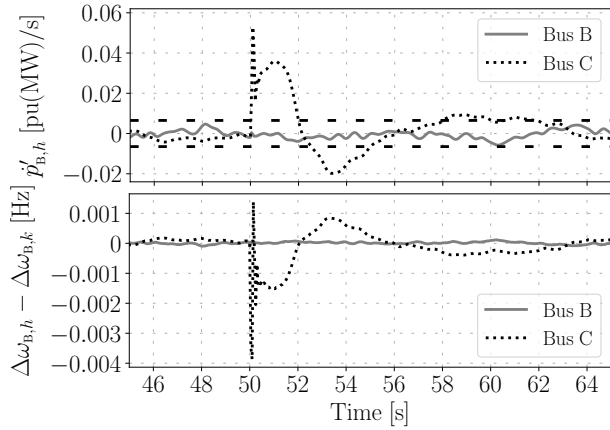


Fig. 14: AIITS – Trajectories of the RoCoP  $\dot{p}'_{B,h}(t)$ , and differences of local and neighboring bus frequency variations at buses B and C following a loss of load (closeup). WECS at bus C includes FFR.

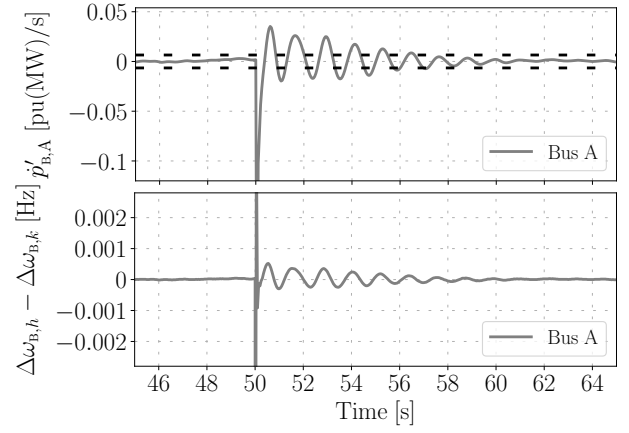


Fig. 15: AIITS – Trajectories of the RoCoP  $\dot{p}'_{B,A}(t)$ , and differences of local and neighboring bus frequency variations at bus A following a loss of load (closeup).

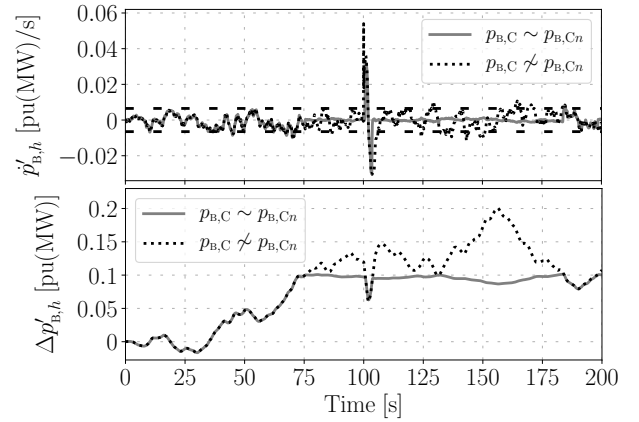


Fig. 16: AIITS – Trajectories of the RoCoP  $\dot{p}'_{B,h}(t)$  and estimated equivalent regulating power at bus C following a loss of load. The WECS operates near its rated power. WECS at bus C includes FFR.

times during the second half of the oscillation. The duration of the overall oscillation is of about 5 seconds, which matches the time windows analyzed in Part I of this paper for the case of the inertial response and PFC of synchronous machines. For the sake of completeness, Fig. 15 shows the RoCoP and frequency variation differences for the synchronous machine at bus A following the loss of the load.

The results discussed so far indicate that measuring the active power injection is, in general, not a sufficient criterion to remunerate the owners of the WECSs for the provision of FFR. The RoCoP appears thus as a valuable tool for system operators. Note that different  $\epsilon_{WT}$  can be defined for different purposes. For instance, the system operator can define a  $\epsilon_{WT,o}$ , common for all devices, above which specific devices are required to provide FFR. Then, individual, possibly multiple thresholds  $\epsilon_{WT,h}$  can be defined for each device or system coupled to FFR.

### C. Case 2: Power Saturation of the WECSs

This section compares the behavior of the RoCoP and of the estimated regulating power variations when the WECS at bus C operates *close* and *far* from its rated power  $p_{B,Cn}$ , and

results are shown in Figs. 16 and 17. The loss of the 44 MW 13.2 MVar load occurs at  $t = 100$  s.

The WECS does not modify its local frequency if operating close to its rated power. Following a disturbance such as the loss of load, the WECS reduces its active power generation, thus impacting on the frequency at its point of connection. A few seconds after the occurrence of the disturbance, the WECS operates again at its rated power and does not impact on the frequency anymore. This example shows that the ability to modify the local frequency is not an intrinsic property of the device itself, but rather, a by-product of its control and operating condition.

### D. Case 3: Measurement Noise

In this last scenario, the robustness of the proposed RoCoP is tested against measurement noise. To this aim, white noise modeled as an Ornstein-Uhlenbeck (mean-reverting) stochastic process is applied to all bus voltage phase angles of the AIITS [33]. The resulting frequency signal shows maximum variations of the order of 5 mHz (see Fig. 18). This value is 5 times higher than the expected maximum PMU error at the fundamental frequency [34]. All measurements are assumed to be of the same technology, thus showing similar noise.

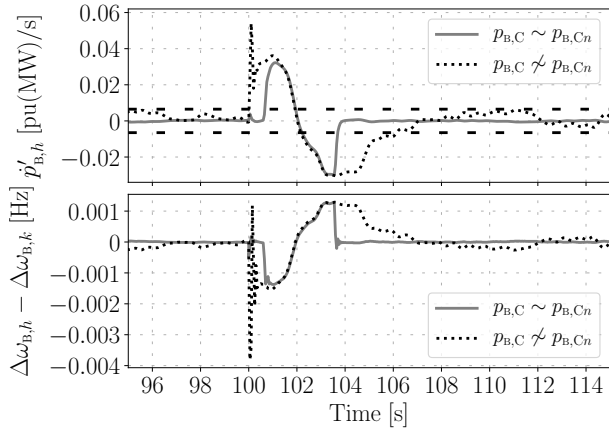


Fig. 17: AIITS – Trajectories of the RoCoP  $\dot{p}'_{B,h}(t)$ , and differences of local and neighboring bus frequency variations at buses B and C following a loss of load (closeup). The WECS operates near its rated power. WECS at bus C includes FFR.

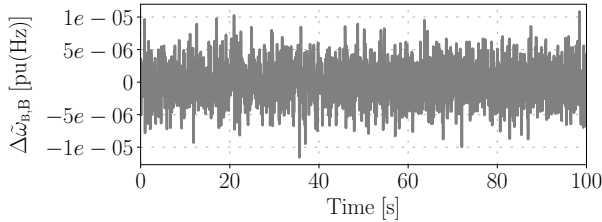


Fig. 18: AIITS – White noise in the frequency signal measured from bus B with a SRF-PLL.

The top-left panel of Fig. 19 shows the trajectories of  $\dot{p}'_{B,h}(t)$  at buses B and C under the presence of noise in the SRF-PLL signals for the same scenario as that of Fig. 13. As expected, the RoCoP is sensitive to fast variations of the frequency signal. With this aim, one can include a Low-Pass Filter (LPF) to *clean* the  $\dot{p}'_{B,h}(t)$  signal. Results obtained with and without the LPF are also shown in Fig. 19.

The RoCoP also shows a relatively high sensitivity to the time constant of the LPF, thus this parameter must be tuned carefully. The ability to distinguish between noise and actual active power variations depends, ultimately on the property of the noise. If the noise has a faster dynamic (i.e., higher autocorrelation coefficient) than the stochastic variations of the power source, in this case, the wind speed, the time constant of the LPF can be tuned so that the noise is filtered out without distorting or over-smoothing the transient behavior of  $\dot{p}'_{B,h}(t)$ . A precise knowledge of the stochastic processes of the sources of the DERs is thus crucial.

The inclusion of a properly tuned LPF thus helps preventing the issues associated to the deterioration of the RoCoP due to the presence of noise in the measurements. The features of the resulting filtered index are fairly similar to those discussed in the previous cases without the presence of noise.

#### E. Spare Remarks

The following remarks are relevant.

1) *Impact of latency*: Latency is a well-known issue when dealing with PMU measurements and communication systems [35]. In this case, however, delays do not prevent the proposed

RoCoP index to be accurate. The calculation of (1), in fact, does not need to be in real-time as it is not utilized for control but, rather, for monitoring and *a posteriori* reward of ancillary services. Since PMU measurements come with a time stamp which is synchronized with the GPS signal, the evaluation of  $\dot{p}'_{B,h}(t)$  is virtually unaffected by communication delays, packet loss, etc.

2) *Impact of the branch impedances on (1)*: The proposed RoCoP index works better the higher are the differences between the frequency variations  $\Delta\omega_{B,h}(t)$  and  $\Delta\omega_{B,k}(t)$  of (1). Note that the inverse of the impedance of the branches (lines or transformers) that connect the monitored bus to the grid ‘amplifies’ such differences. If a branch impedance is too small and, hence, the accuracy with which frequency variations have to be measured is too high, one can utilize measurements at further buses as described in the discussion of equation (33) in Part I.

3) *Impact of the time integration step on (1)*: The performance of the proposed index does not depend on the time integration step of the simulations that were carried out and presented in this paper, as long as such integration step is sufficiently small to capture the dynamics of interest. This is shown in Fig. 20, where the same scenario as that of the bottom-left panel of Fig. 19 is considered for different time steps namely 50, 10 and 100 ms. These results are substantially the same regardless of the time step used, even for a difference of one order of magnitude of its value.

Taking into account the fact that the range of time integration steps considered in the example above lie in the typical sampling rates of measurement devices currently deployed, then this remark can be extended to real-life scenarios. In other words, the performance of the proposed RoCoP index is independent of the sampling rate of measurement units.

## VI. CONCLUSIONS

The second part of this paper presents an index that allows understanding whether a non-synchronous device provides frequency control and/or inertial response following a power unbalance. Simulation results confirm the accuracy and the robustness of the proposed approach. The proposed approach appears to have great potential for practical applications. The index and the ‘regulating power,’ in fact, can be calculated with measurements and data that are available to the TSOs. No confidential measurement or data have to be obtained from the monitored devices.

Future work will focus on the practical implementation of the RoCoP index. For example, proper techniques to transmit measurement data without saturating the bandwidth and to filter noise need to be thoroughly designed and tested. Future stages of this research will also involve the analysis of the accuracy and utility of the proposed methodology considering field trials with real grid measures.

## ACKNOWLEDGMENTS

The authors wish to thank Dr. Ivan Dudurich with EirGrid Group, Ireland, and all the people with TransElectrica, Romania, that participated in the EU project RESERVE, for the

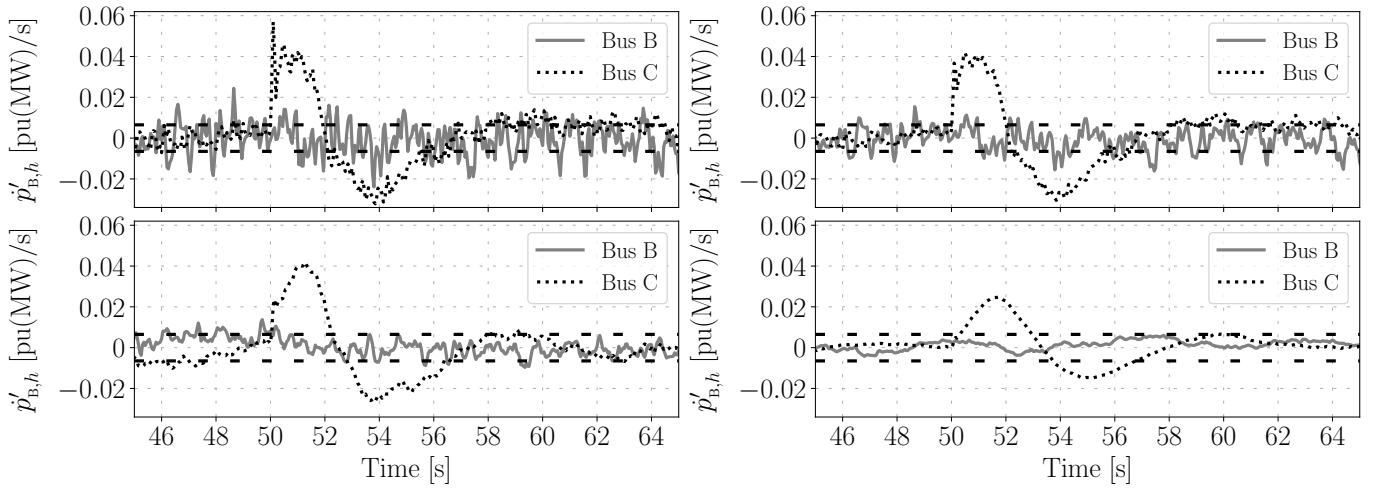


Fig. 19: AIITS – RoCoP at buses B and C following a loss of load with noisy frequency measurements. WECS at bus C includes FFR (closeup). Top-left panel: No filter. Top-right panel: LPF with time constant 0.5 ms. Bottom-left panel: LPF with time constant 1 ms. Bottom-right panel: LPF with time constant 5 ms.

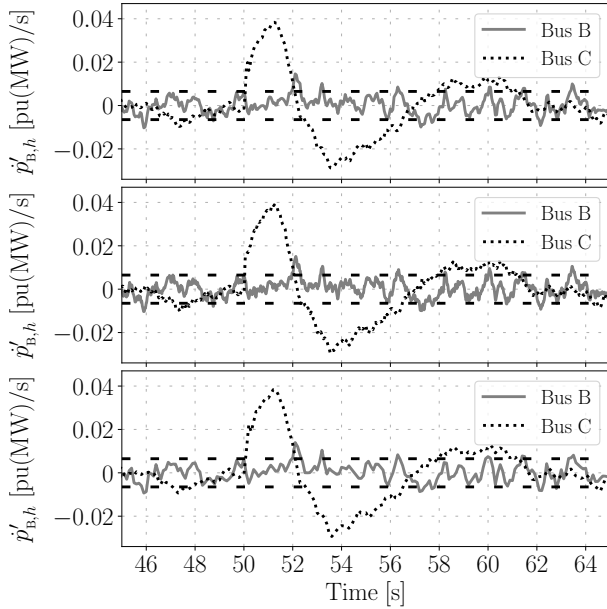


Fig. 20: AIITS – RoCoP at buses B and C following a loss of load for different time integration steps,  $\Delta T_{st}$ . WECS at bus C includes FFR. From top to bottom:  $\Delta T_{st}=50$  ms;  $\Delta T_{st}=10$  ms;  $\Delta T_{st}=100$  ms.

discussions on the monitoring, control and ancillary service reward policies of non-synchronous devices.

## REFERENCES

- [1] H. F. Illian, "Frequency control performance measurement and requirements," Lawrence Berkeley National Laboratory, Berkeley, Tech. Rep. LBNL-4145E, 2010.
- [2] C. S. Xue and M. Martinez, "Review of the recent frequency performance of the Eastern, Western and ERCOT interconnections," Lawrence Berkeley National Laboratory, Berkeley, Tech. Rep. LBNL-4144E, 2010.
- [3] F. Milano, F. Dörfler, G. Hug, D. J. Hill, and G. Verbič, "Foundations and challenges of low-inertia systems (invited paper)," in *Power Systems Computation Conference (PSCC)*, Dublin, Ireland, Jun. 2018, pp. 1–25.
- [4] K. Samarakoon, J. Ekanayake, and N. Jenkins, "Investigation of domestic load control to provide primary frequency response using smart meters," *IEEE Trans. on Smart Grid*, vol. 3, no. 1, pp. 282–292, Mar. 2012.
- [5] J. Morren, S. W. H. de Haan, W. L. Kling, and J. A. Ferreira, "Wind turbines emulating inertia and supporting primary frequency control," *IEEE Trans. on Power Systems*, vol. 21, no. 1, pp. 433–434, Feb. 2006.
- [6] V. Gevorgian, Y. Zhang, and E. Ela, "Investigating the impacts of wind generation participation in interconnection frequency response," *IEEE Trans. on Sustainable Energy*, vol. 6, no. 3, pp. 1004–1012, Jul. 2015.
- [7] J. Boyle, T. Littler, and A. Foley, "Review of frequency stability services for grid balancing with wind generation," *The Journal of Engineering*, vol. 2018, no. 15, pp. 1061–1065, 2018.
- [8] H. Asano, K. Yajima, and Y. Kaya, "Influence of photovoltaic power generation on required capacity for load frequency control," *IEEE Trans. on Energy Conversion*, vol. 11, no. 1, pp. 188–193, Mar. 1996.
- [9] N. Kakimoto, S. Takayama, H. Satoh, and K. Nakamura, "Power modulation of photovoltaic generator for frequency control of power system," *IEEE Trans. on Energy Conversion*, vol. 24, no. 4, pp. 943–949, Dec. 2009.
- [10] A. Elrayyah, Y. Sozer, and M. E. Elbuluk, "Modeling and control design of microgrid-connected PV-based sources," *IEEE Journal of Emerging and Selected Topics in Power Electronics*, vol. 2, no. 4, pp. 907–919, Dec. 2014.
- [11] M. Guan, J. Cheng, C. Wang, Q. Hao, W. Pan, J. Zhang, and X. Zheng, "The frequency regulation scheme of interconnected grids with VSC-HVDC links," *IEEE Trans. on Power Systems*, vol. 32, no. 2, pp. 864–872, Mar. 2017.
- [12] A. Oudalov, D. Chartouni, and C. Ohler, "Optimizing a battery energy storage system for primary frequency control," *IEEE Trans. on Power Systems*, vol. 22, no. 3, pp. 1259–1266, Aug. 2007.
- [13] Á. Ortega and F. Milano, "Modeling, simulation, and comparison of control techniques for energy storage systems," *IEEE Trans. on Power Systems*, vol. 32, no. 3, pp. 2445–2454, May 2017.
- [14] J. W. Shim, G. Verbič, N. Zhang, and K. Hur, "Harmonious integration of faster-acting energy storage systems into frequency control reserves in power grid with high renewable generation," *IEEE Trans. on Power Systems*, vol. 33, no. 6, pp. 6193–6205, Nov. 2018.
- [15] M. Cheng, J. Wu, S. J. Galsworthy, C. E. Ugalde-Loo, N. Gargov, W. W. Hung, and N. Jenkins, "Power system frequency response from the control of bitumen tanks," *IEEE Trans. on Power Systems*, vol. 31, no. 3, pp. 1769–1778, May 2016.
- [16] E. Vrettos, C. Ziras, and G. Andersson, "Fast and reliable primary frequency reserves from refrigerators with decentralized stochastic control," *IEEE Trans. on Power Systems*, vol. 32, no. 4, pp. 2924–2941, Jul. 2017.
- [17] I. Beil, I. Hiskens, and S. Backhaus, "Frequency regulation from commercial building HVAC demand response," *Procs of the IEEE*, vol. 104, no. 4, pp. 745–757, Apr. 2016.
- [18] EirGrid and SONI, "All-island ten year transmission forecast statement 2017," 2018. [Online]. Available: <http://www.eirgridgroup.com/site-files/library/EirGrid/TYTF5-2017-Final.pdf>
- [19] M. A. A. Murad, G. Tzounas, M. Liu, and F. Milano, "Frequency control through voltage regulation of power system using svc devices," in *IEEE PES General Meeting (PESGM)*, 2019, pp. 1–5.

- [20] F. Milano, "A Python-based software tool for power system analysis," in *Procs of the IEEE PES General Meeting*, Vancouver, BC, July 2013.
- [21] F. Milano and Á. Ortega, *Converter-Interfaced Energy Storage Systems: Context, Modelling and Dynamic Analysis*. Cambridge, UK: Cambridge University Press, 2019.
- [22] S. Kundu, N. Sinitzyn, I. Hiskens, and S. Backhaus, "Modeling and control of thermostatically controlled loads," in *Power Systems Computation Conference (PSCC)*, Stockholm, Sweden, 2011, pp. 969–975.
- [23] H. Zhao, Q. Wu, S. Huang, H. Zhang, Y. Liu, and Y. Xue, "Hierarchical control of thermostatically controlled loads for primary frequency support," *IEEE Trans. on Smart Grid*, vol. 9, no. 4, pp. 2986–2998, July 2018.
- [24] J. L. Mathieu, S. Koch, and D. S. Callaway, "State estimation and control of electric loads to manage real-time energy imbalance," *IEEE Trans. on Power Systems*, vol. 28, no. 1, pp. 430–440, 2013.
- [25] J. M. Mauricio, A. Marano, A. Gómez Expósito, and J. L. Martínez Ramos, "Frequency regulation contribution through variable-speed wind energy conversion systems," *IEEE Trans. on Power Systems*, vol. 24, no. 1, pp. 173–180, Feb 2009.
- [26] J. Ekanayake and N. Jenkins, "Comparison of the response of doubly fed and fixed-speed induction generator wind turbines to changes in network frequency," *IEEE Trans. on Energy Conversion*, vol. 19, no. 4, pp. 800–802, Dec. 2004.
- [27] G. M. Jónsdóttir, B. Hayes, and F. Milano, "Optimum data sampling frequency for short-term analysis of power systems with wind," in *IEEE PES General Meeting*, Aug 2018, pp. 1–5.
- [28] G. M. Jónsdóttir and F. Milano, "Data-based continuous wind speed models with arbitrary probability distribution and autocorrelation," *Renewable Energy*, vol. 143, pp. 368 – 376, 2019.
- [29] G. M. Jónsdóttir, B. Hayes, and F. Milano, "Modeling solar irradiance for short-term dynamic analysis of power systems," in *IEEE PES General Meeting*, Aug 2019, pp. 1–5.
- [30] G. M. Jónsdóttir and F. Milano, "Modeling of short-term tidal power fluctuations," *IEEE Trans. on Sustainable Energy*, pp. 1–1, 2019.
- [31] R. Zárate Miñano and F. Milano, "Construction of SDE-based wind speed models with exponentially decaying autocorrelation," *Renewable Energy*, vol. 94, pp. 186 – 196, 2016.
- [32] P. W. Sauer and M. A. Pai, *Power System Dynamics and Stability*. Upper Saddle River, NJ: Prentice Hall, 1998.
- [33] F. Milano and R. Zárate Miñano, "A systematic method to model power systems as stochastic differential algebraic equations," *IEEE Trans. on Power Systems*, vol. 28, no. 4, pp. 4537–4544, Nov 2013.
- [34] A. Derviškadić, P. Romano, and M. Paolone, "Iterative-interpolated DFT for synchrophasor estimation: A single algorithm for P- and M-class compliant PMUs," *IEEE Trans. on Instrumentation and Measurement*, vol. 67, no. 3, pp. 547–558, March 2018.
- [35] M. Liu, I. Dassios, G. Tzounas, and F. Milano, "Stability analysis of power systems with inclusion of realistic-modeling WAMS delays," *IEEE Trans. on Power Systems*, vol. 34, no. 1, pp. 627–636, Jan 2019.



**Federico Milano** (S'02, M'04, SM'09, F'16) received from the University of Genoa, Italy, the ME and Ph.D. in Electrical Engineering in 1999 and 2003, respectively. From 2001 to 2002, he was with the Univ. of Waterloo, Canada. From 2003 to 2013, he was with the Univ. of Castilla-La Mancha, Spain. In 2013, he joined the Univ. College Dublin, Ireland, where he is currently Professor of Power Systems Control and Protections and Head of Electrical Engineering. His research interests include power systems modeling, control and stability analysis.



**Álvaro Ortega** (S'14, M'16) received the degree in Industrial Eng. from Escuela Superior de Ingenieros Industriales, Univ. of Castilla-La Mancha, Ciudad Real, Spain, in 2013. In 2017, he received the Ph.D. in Electrical Eng. from Univ. College Dublin, Ireland, where he stayed until 2019. In 2020, he joined the **LOYOLATech** institute in Universidad Loyola Andalucía, where he practices as senior power systems researcher. His current current fields of research include modeling, control and stability of energy storage systems; frequency estimation,

control and stability in low-inertia systems; and design of advanced monitoring and control systems for flexible energy grids.